Carbon Trends 18 (2025) 100447

Contents lists available at ScienceDirect

Carbon Trends

journal homepage: www.elsevier.com/locate/cartre

In-situ electrochemical fabrication of holey graphene oxide and oxo-functionalized graphene for electrochemical sensing

Gang Li [a,b,1], Ming Qin [a,1], Qiang Zhang [a], Baiqing Yuan [a,*], Lanxin Xue [a], Shuning Zhang [a], Jingfei Yan [a], Chunying Xu [a,*]

[a] School of Chemistry and Materials Science, Ludong University, Yantai 264025, Shandong, China
[b] College of Science and Engineering, James Cook University, Townsville 4811, QLD, Australia

ARTICLE INFO

Keywords:
Holey graphene oxide (HGO)
Oxo-functionalized graphene
Electrochemically oxidized graphene oxide (EOGO)
Electrochemical sensing
Anti-fouling

ABSTRACT

The in-situ electrochemical generation method streamlines the synthesis of active materials directly onto the electrode surface, which enhances the electrical connection and minimizes interface resistance. This approach not only simplifies the modification process but also significantly enhances signal stability and reproducibility in electrochemical sensing. Here, holey graphene oxide and oxo-functionalized graphene were in-situ generated by an electrochemical method in a green and mild solution. The active interfaces were explored for the electrochemical sensing of dopamine, ascorbic acid and uric acid, focusing on electroactivity, antifouling, selectivity, and background noise. Findings reveal the crucial role of oxo-functional groups and defects at the interfaces in determining the sensor's performance, highlighting a trade-off between high sensitivity and antifouling capability/selectivity.

1. Introduction

Electrochemical sensors are renowned for their swift and precise detection of a wide array of analytes, making them extensively utilized in fields such as environmental monitoring [1], agricultural analysis [2], food safety [3], and biomedical applications [4]. Particularly in medical diagnostics, electrochemical sensors emerge as a promising option due to their affordability, quick response, high sensitivity and selectivity, the feasibility of miniaturization and portability, and the capability for point-of-care testing in real-time [5–7]. An ideal nonenzymatic electrochemical sensor for practical applications is supposed to possess excellent electrocatalytic activity, good selectivity and antifouling properties simultaneously, however, attaining this combination is exceedingly challenging. It is widely acknowledged that the most straightforward and effective strategy for improving the electrochemical performance of sensors involves modifying the electrode surface with materials that are both highly active and resistant to fouling [8]. For example, Qiao developed an electrochemical sweat sensor using a hydrogel composed of gold nanoparticles (AuNPs), molybdenum disulfide (MoS_2), and peptides (Pep). The sensor demonstrated exceptional anti-biofouling capabilities and was capable of selectively detecting uric acid (UA) and ascorbic acid (AA) in real sweat samples [9]. Zhu developed an electrochemical sensor that combines three-dimensional macroscopic graphene (3DG) with a vertically-ordered mesoporous silica-nanochannel film (VMSF), resulting in the VMSF/pl-3DG sensor. This sensor demonstrated rapid and ultra-sensitive detection of UA in complex samples, along with outstanding antifouling and anti-interference capabilities [10]. Similarly, Zhang et al. constructed an anti-fouling electrochemical sensor for dopamine (DA) detection, achieving remarkable stability and anti-fouling performance by integrating single-layer MXene (S-MXene) with holey graphene (HG) [11]. Despite the impressive electrochemical performance of these sensors in detecting electroactive biomolecules, their composite materials' preparation processes are often expensive, complex, and time-consuming. Consequently, there is a critical need to develop an electrochemical sensor that is not only simple, cost-effective, and efficient but also exhibits high electrocatalytic activity and effective antifouling properties. Graphene, characterized by a single layer of sp2 hybridized carbon atoms organized in a hexagonal lattice, stands out as a distinctive two-dimensional (2D) carbon nanomaterial [12]. Its remarkable chemical and physical attributes have led to significant applications across various fields, including energy storage, drug delivery, biomedicine,

* Corresponding authors.
E-mail addresses: bqyuan@ldu.edu.cn (B. Yuan), chunyingxu@ldu.edu.cn (C. Xu).
[1] These authors contributed equally to this work.

https://doi.org/10.1016/j.cartre.2024.100447
Received 26 June 2024; Received in revised form 15 December 2024; Accepted 17 December 2024
Available online 18 December 2024

environmental science, gas adsorption, and electrochemical sensing [13–15]. However, pristine graphene sheets might display limited efficiency in electrocatalysis and electroanalysis. It has been reported that some oxygen-containing functional groups and defects on the surface of graphene played vital roles in electrocatalytic activity, selectivity and anti-fouling properties [16,17]. Graphene oxide (GO), a common derivative of graphene, is characterized by a mix of sp2 and sp3 carbon regions within a single graphene layer. Furthermore, GO's surface is rich in various oxygen functional groups, including hydroxyl (C—OH), epoxy (C—O-C), carboxylic acid (O═C—OH or its salt), and ketone (C═O) [18, 19]. The functional groups present significantly affect the structure and properties of GO. Presently, the primary synthesis methods for GO include those developed by Brodie, Staudenmaier, Hofmann, Hummers, and Tour [20]. These diverse preparation techniques result in GO variants with different oxygen functional groups and levels of oxidation [21]. Additionally, GO can be transformed into reduced GO (RGO) through various reduction methods, including chemical reduction, thermal reduction (encompassing thermal annealing, hydrothermal, and solvothermal techniques), photoreduction, and electrochemical reduction [22,23]. For instance, Liu [24] introduced a chemical processing method that utilizes hydroiodic (HI) acid solution to precisely adjust the oxygen content in RGO. This approach to modifying RGO's oxygen levels opens the door to a broad range of applications, each benefiting from the material's specific oxygen content.

Recently, holey GO (HGO) has gained increasing attention due to its numerous defect densities and high active surface area. Zakaria et al. developed an effective method for generating HGO by electrochemical reduction of GO and subsequently the oxidation of RGO [25]. The synthesized HGO provided an ideal platform for modifying β-Cyclodextrin (β-CD), which exhibited outstanding electrocatalytic activity for the discriminated oxidation of DA. Gregg et al. also reported the enzymatic oxidation of GO by horseradish peroxidase (HRP), resulting in the formation of holes on its basal plane [26]. However, these preparation methods are often complex, time-consuming, and uncontrollable. Hence, there is still a need for a simple, environmentally friendly, efficient, and affordable approach to accurately control the formation of holes on the surface of GO. Recently, our group has studied electrochemically oxidized graphene oxide (EOGO) and found that HGO may be generated on the surface of GO through a gentle and eco-friendly electrochemical oxidation process [27]. The HGO demonstrated remarkable electrocatalytic performance and resistance to fouling in detecting UA within actual human serum samples. Furthermore, extensive research has highlighted that electrochemical activation of glassy carbon electrodes (GCE) can enhance their electrocatalytic capabilities by introducing various oxygen-containing functional groups [28–30]. Santhiago et al. introduced a novel approach for the electrochemical formation of an oxidized carbon surface from GCE [31]. This method yields a material that exhibits a similar electrochemical behavior comparable to GO. Similarly, Our group have demonstrated the in-situ formation of oxo-functionalized graphene structures on the surface of a GCE and its subsequent application [32]. This process involves electrochemical oxidation followed by a reduction method. Additionally, Wei et al. presented an efficient method for synthesizing nano-graphene oxide (NGO) with adjustable sizes and a range of oxygen functional groups through a one-step of water electrolytic oxidation of GCE in sulfuric acid [33]. This NGO demonstrates a high level of oxidation and excellent dispersion stability, making it particularly effective for oxidizing benzylamine and benzene. Considering the disordered graphitic structure of the GCE, where nanosized graphite sheets are intertwined compactly in random orientations, it is plausible that micro-regional oxo-functionalized graphene was generated on the GCE surface [32,34]. In essence, the electrochemical approach offers a swift, straightforward, environmentally friendly, and highly effective means of manipulating the oxygen functional groups on the electrode's surface.

In the study, HGO and oxo-functionalized graphene were in-situ generated using an electrochemical method conducted in a mild and eco-friendly solution. The in-situ electrochemical generation method stands out for its ability to directly generate active materials on the electrode surface, which simplifies the modification process, enhances signal stability and reproducibility, improves electrical connections, reduces interface resistance, and ultimately, elevates the performance of electrochemical sensors. These advantages make it a strong contender among the various oxygen functionalization methods available [35–37]. In addition, in order to address the gaps in the current literature and to provide a thorough understanding of the role of GO and its derivatives in the field of electrochemical sensing. we have conducted an in-depth examination of various electrode interfaces, encompassing GO, electrochemically oxidized GO (referred to as holey GO or EHGO), electrochemically reduced GO, and oxo-functionalized graphene generated directly on GCE. We concentrated on assessing the electrocatalytic performance, selectivity, anti-fouling attributes, and background signal interference for the determination of UA, DA, and AA using these diverse electrode interfaces. These substances are typically challenging to differentiate in electrochemical sensing due to their similar electrochemical behaviors. The detailed investigation provided insights into the potential of these materials in enhancing the analytical capabilities of electrochemical sensors, offering promising avenues for sensitive and selective detection of these biologically important compounds. HGO was produced directly via electrochemical oxidation of GO/GCE, with the resulting material being named EHGO. The oxidation formation mechanism of EHGO was analyzed in detail using cyclic voltammetry (CV). The electrodes preparation and electrochemical sensing process are illustrated in Scheme 1.

This study thoroughly investigates the electroactivity, selectivity, anti-fouling properties, and background noise in electrochemical sensing of UA, DA, and AA using EHGO and oxo-functionalized graphene electrodes. Scheme 2 shows the electro-oxidation mechanism of UA, AA, and DA. In order to investigate the properties of the electrode interface, various analytical techniques were employed including contact angle measurement, scanning electron microscopy (SEM), Raman spectroscopy, and Electrochemical impedance spectra (EIS). The analytical performance of electrodes was evaluated through differential pulse voltammetry (DPV). The EHGO displayed excellent selectivity, electrocatalytic properties and robust antifouling properties for the determination of UA, DA, and AA in real human serum samples, while the oxo-functionalized graphene electrodes exhibited higher sensitivity.

2. Experimental

2.1. Chemicals and solutions

UA, DA, and AA were purchased from Sigma-Aldrich, located in St. Louis, MO, USA. A GO aqueous suspension, with a concentration of 5.0 mg/mL, was acquired from Nanjing XFNano Materials Tech Co., Ltd, based in Nanjing, Jiangsu, China, known for their high-grade materials. The rest of the chemicals, all of analytical grade, were utilized as received without any additional purification steps. Ultrapure deionized water, boasting a resistivity of 18.25 MΩ·cm, served as the solvent for all aqueous solutions prepared during the study. Human serum, obtained from a healthy male volunteer at Ludong University Hospital, was used for the real sample tests.

2.2. Apparatus

The electrodes' surface morphologies were examined using a Hitachi Regulus 8100 SEM from Tokyo, Japan, providing detailed imagery crucial for our analysis. Surface wettability was quantified through water contact angles (CAs), measured with precision by the JC2000 Instrument from Shanghai Zhongchen Instrument Co., China. Elemental composition and chemical states were determined using X-ray photoelectron spectroscopy (XPS) on a Thermo ESCALAB 250 Xi spectrometer

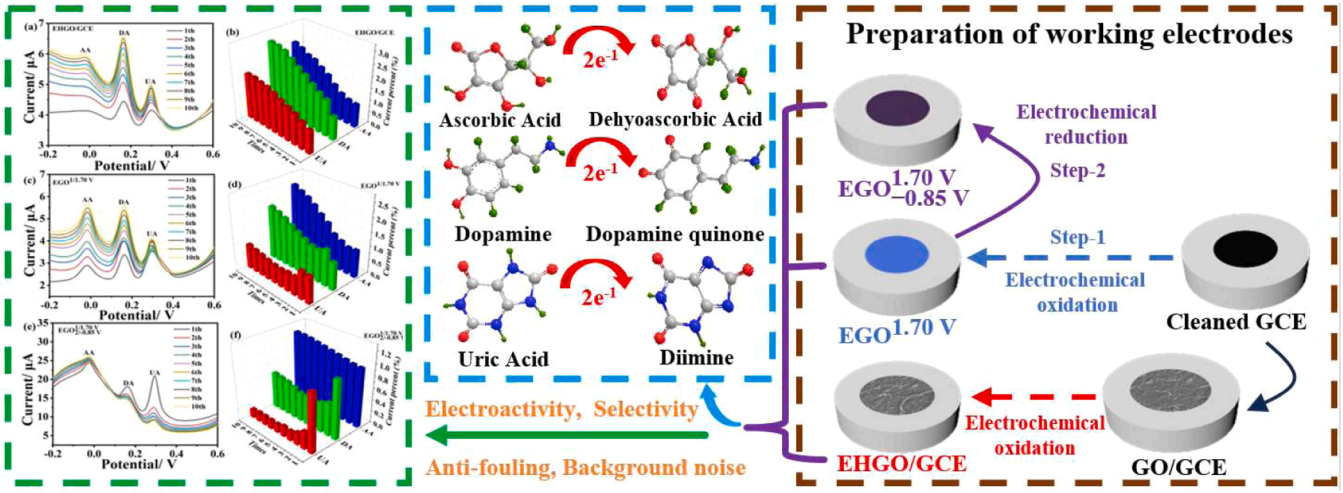

Scheme 1. The fabrication of three electrochemical interfaces and an investigation into their analytical performances for the determination of AA, UA, and DA.

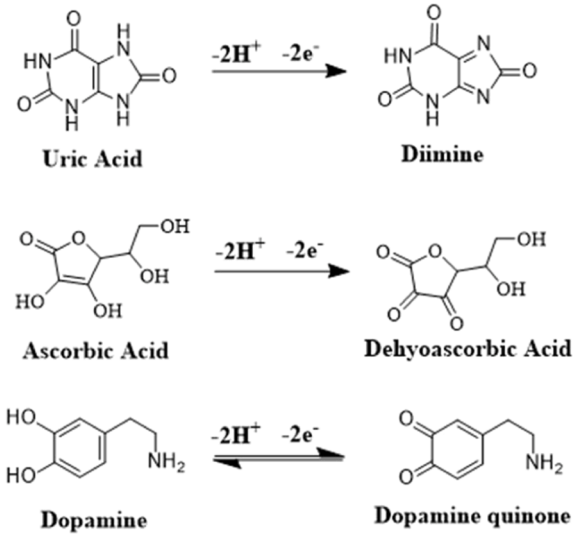

Scheme 2. The electro-oxidation mechanism of UA, AA, and DA.

from Waltham, MA, USA, equipped with a monochromatic Al Kα X-ray source. The molecular structure was probed using a LabRAM HR Evolution high-resolution Raman spectrometer by HORIBA Scientific, Palaiseau, France, utilizing a 532 nm laser for excitation. Electrochemical behaviors were thoroughly investigated using a CHI 750E electrochemical workstation from Shanghai CH Instrument Co., Ltd., China, employing a conventional three-electrode system. This setup included a working electrode, a platinum coil auxiliary electrode, and an Ag/AgCl reference electrode in a saturated KCl solution. EIS was conducted in a 0.1 M KCl solution containing 5 mM of $Fe(CN)_6^{3-/4-}$ across a frequency range of 1 MHz to 0.1 Hz at an applied potential of 0.25 V. DPV analyses were performed over a potential range from −0.4 to 0.6 V.

2.3. Electrode preparation and modification

Before its modification, the GCE with a diameter of 3 mm and an area of 0.07 cm^2 was meticulously polished to achieve a mirror-like surface. This was accomplished through a graduated polishing process using alumina powders with particle sizes of 1, 0.3, and 0.05 μm, respectively. Following the polishing stage, the electrode was extensively washed with ultrapure deionized water followed by ethanol to remove any residual polishing agents or contaminants.

To prepare the GO coating solution, 100 μL of a GO aqueous solution (concentration: 5.0 mg/mL) was first diluted to 500 μL using deionized water. Subsequently, the solution was sonicated using an ultrasonic instrument (provided by Shanghai Kedao Ultrasonic Instrument Co., Ltd) at a power setting of 100 W and a temperature of 25 °C for 10 min, resulting in a 1 mg/mL GO solution.

The GO-modified GCE (GO/GCE) was then prepared by carefully depositing 5.0 μL of the sonicated GO suspension (1.0 mg/mL) onto the surface of the cleaned GCE. This assembly was left to dry at room temperature, ensuring a uniform coating of GO on the electrode surface.

The electrochemical treatment of GCE and GO/GCE was conducted under various conditions, leading to the creation of several distinct electrode modifications, each denoted with specific labels to reflect their treatment process.

(1) Electrochemical treatment in NaOH and H_2SO_4:
The GCE and GO/GCE were treated in 0.1 M NaOH and 0.1 M H_2SO_4 solutions by applying a range of potentials (1.35–1.75 V) for 500 s through an i-t curve. These treated electrodes were labeled as NaOH-$GCE^{1/potential}$, NaOH-$GO^{1/potential}$, H_2SO_4-$GCE^{1/potential}$, and H_2SO_4-$GO^{1/potential}$.

(2) Electrochemical oxidation in PBS:
The GCE and GO/GCE underwent electrochemical oxidation in 0.1 M phosphate buffer solution, applying various potentials (1.60–1.85 V) for 500 s. The resulting electrodes were termed as $EGO_{1/potential}$ and $EHGO/GCE^{1/potential}$, respectively. Specifically, oxidation at 1.70 V resulted in electrodes referred to as $EGO^{1/1.70\ V}$ and EHGO/GCE for GCE and GO/GCE, respectively. Unless otherwise specified, the buffer solution refers to 0.1 M PBS (pH=7.0)

(3) Electrochemical oxidation followed by reduction:
An electrode oxidized at 1.70 V and then reduced at various potentials was labeled as "$EGO^{1/1.70\ V}_{2/potential}$". Conversely, an electrode oxidized at various potentials before being reduced at −0.85 V was designated as "$EGO^{1/potential}_{2/-0.85\ V}$". The specific process of oxidizing the GCE in 0.1 M PBS at 1.70 V followed by reduction in 0.1 M ABS (pH = 4.0) at −0.85 V is denoted as "$EGO^{1/1.70\ V}_{2/-0.85\ V}$". Unless otherwise specified, the buffer solution refers to 0.1 M PBS (pH=7.0).

(4) $GO_{-0.75}$/GCE: The GO/GCE was electrochemically reduced in a 0.1 M acetate buffer solution (ABS, pH = 4.0) at a potential of −0.75 V for 500 s.

3. Results and discussion

3.1. Electrode characterization

The morphological features of various electrodes are shown in **Fig S1.** Sample (a) depicts a standard GCE with its inherent glossy black appearance, indicative of its pristine condition. Sample (b), $EGO^{1/1.70V,}$ shows a distinctive blue tint, resulting from the electrochemical oxidation at 1.70 V, which could imply a surface modification by oxide formation. Sample (c), $EGO^{1/1.70\ V}_{2/-0.85\ V}$features a gradient of taupe from the center towards the edge, reflecting the dual electrochemical reduction of $EGO^{1/1.70V}$, hinting at a complex multilayer structure. Sample (d) exhibits a dark brown characteristic of a GO coating on the GCE. Finally, sample (e), EHGO/GCE also shows a brown dark surface but much darker than GO/GCE. The EHGO/GCE is also characterized by SEM (**Fig S2a, b**), showing remarkably wrinkled and rippled structures, similar to that of GO.

The hydrophilicity and hydrophobicity of different electrode surfaces were evaluated using static water contact angle measurements. Fig. 1 shows the static CAs of (a) GCE, (b) $EGO^{1/1.70\ V}$, (c) $EGO^{1/1.70\ V}_{2/-0.85\ V}$, (d) GO/GCE and (e) EHGO/GCE. The water CA of GCE measured approximately 80.78° Upon electrochemical oxidation of GCE to form $EGO^{1/1.70\ V}$, the water CA decreased to 47.89°, indicating a hydrophilic surface owing to the increased oxo-functional groups such as hydroxyl, carbonyl, carboxyl, and oxide groups [38]. Subsequent electrochemical reduction of $EGO^{1/1.70\ V}$ to $EGO^{1/1.70\ V}_{2/-0.85\ V}$, resulted in an increase in water CA to 54.93°, reflecting partial reduction of the oxo-functional groups on the electrode surface. The GO/GCE displayed a water CA of 27.19°, indicating a more hydrophilic surface because of the abundant oxo-functional groups on its basal plane and edges. EHGO/GCE demonstrated a water CA of 29.72°, nearly unchanged in hydrophilicity compared to GO/GCE. Thus, the results suggest that the content of oxo-functional groups on the electrode surfaces follows the order: GO/GCE > EHGO/GCE > $EGO^{1/1.70\ V}$ > $EGO^{1/1.70\ V}_{2/-0.85\ V}$ > GCE. Oxo-functional groups have been shown to significantly enhance the electrocatalytic activity and antifouling ability of electrode surfaces [39].

The elemental composition and chemical states of these electrodes were further analyzed by XPS. The XPS survey spectrum depicted in Fig. S3 prominently features the signature peaks of carbon (C), nitrogen (N), and oxygen (O) elements. Analysis of the XPS survey scans reveals a notable increase in the intensity of the O 1 s peak for the GCE that has been subjected to electrochemical oxidation ($EGO^{1/1.70\ V}$), compared to the untreated, bare GCE, confirming the effectiveness of the oxidation process. **Fig. S4** shows the C 1 s XPS spectra of GCE, $EGO^{1/1.70\ V}$, $EGO^{1/1.70\ V}_{2/-0.85\ V}$, GO, and EHGO. For GCE, the spectra exhibit three peaks associated with C═C/C—C, C—O, and C═O at 284.18, 285.01, and 288.11 eV, respectively. In contrast, the spectra of the other four electrodes show five peaks attributed to C═C/C—C, C—O, C═O, and O—C═O at different binding energies [40]. **Table S-1** presents the fitted parameters for C 1 s XPS spectra. Compared to GCE, $EGO^{1/1.70\ V}$ exhibits a higher amount of C═O and O—C═O groups, and a decrease in the amount of C—O group due to electrochemical oxidation. Subsequent electrochemical reduction of EGO1/1.70 V to $EGO^{1/1.70\ V}_{2/-0.85\ V}$ results in a decrease in the concentration of O-C═O and C═O groups. EHGO, compared to GO, shows an increase in the concentration of C = C/C—C but a decrease in the concentration of C—O, C═O, and O—C═O groups, indicating destruction of oxo-functional groups under high potential. **Fig. S5** shows the O 1 s XPS spectra of GCE, $EGO^{1/1.70\ V}$, $EGO^{1/1.70\ V}_{2/-0.85\ V}$, GO, and EHGO. The O 1 s spectra of these samples exhibit four divided peaks at 530.91–530.99, 531.87–532.13, 532.60–532.89, and 533.40–533.86 eV, corresponding to O-C═O, C═O, C—OH, and C—O-C, respectively [41]. Moreover, the O 1 s spectra of $EGO^{1/1.70\ V}$, $EGO^{1/1.70\ V}_{2/-0.85\ V}$ and EHGO show an additional fitted peak at 535.68–535.98 eV, which may be assigned to chemisorbed oxygen or water. **Table S-2** shows the fitted parameters for O 1 s XPS spectra. The N 1 s XPS spectra of GCE, $EGO^{1/1.70\ V}$, $EGO^{1/1.70\ V}_{2/-0.85\ V}$, GO, and EHGO (**Fig. S6**) show a single peak at 399.86–401.40 eV (-NH) [42]. Similarly, the S 2p spectra (**Fig. S7**) exhibit a single peak at 167.68–168.46 eV ($-SO_3H$) [43]. The P 2p XPS spectra of GCE, $EGO^{1/1.70\ V}_{2/-0.85\ V}$ and GO (**Fig. S8a, c, d**) exhibited one small peak at 133.48–133.99 eV ($2P_{2/3}$). However, For $EGO^{1/1.70\ V}$ and EHGO (**Fig. S8b, e**), the P 2p XPS spectra displayed two peaks at 132.87–133.96 eV ($2P_{2/3}$ and $2P_{1/2}$), This indicated that the electrochemical oxidation process resulted in phosphorus modification due to the presence of phosphates in PBS [44].

Raman spectroscopy is a rapid, accurate, and highly reliable technique for investigating the defect density within carbon frameworks. Fig. 2 shows the deconvoluted Raman spectra of (a) GO/GCE, (b) EHGO/GCE, (c) $EGO^{1/1.70\ V}$, and (d) $EGO^{1/1.70\ V}_{2/-0.85\ V}$. The low-wavenumber region was fitted by five peaks, namely D*, D, D″, G, and D′ bands, while the high-wavenumber region is characterized by four peaks encompassing G*, 2D, $D + D'$, and 2D′ bands, as illustrated in Fig. 2. The fitted detailed parameters of all bands are summarized in **Tables S3** and **S4**. The D* band, appearing at ~1134–1156 cm^{-1} in all the spectra, is attributed to sp^2-sp^3 bonds stretching vibrations of disordered graphitic lattices [45]. Principal peaks centered at approximately 1345–1350 cm^{-1} and 1578–1591 cm^{-1} correspond to the D and G bands, respectively. The D band is associated with various defects in the graphite material such as bond-angle disorder, bond-length disorder, vacancies, and edge defects [46], whereas the G band is due to the E2 g mode of graphite and

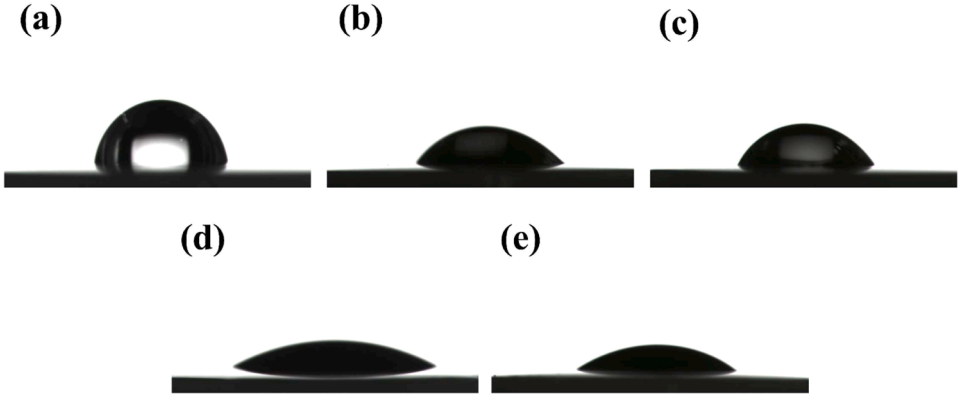

Fig. 1. Contact angle images of water on (a) GCE, (b) $EGO^{1/1.70\ V}$, (c) $EGO^{1/1.70\ V}_{2/-0.85\ V}$, (d) GO/GCE, and (e) EHGO/GCE.

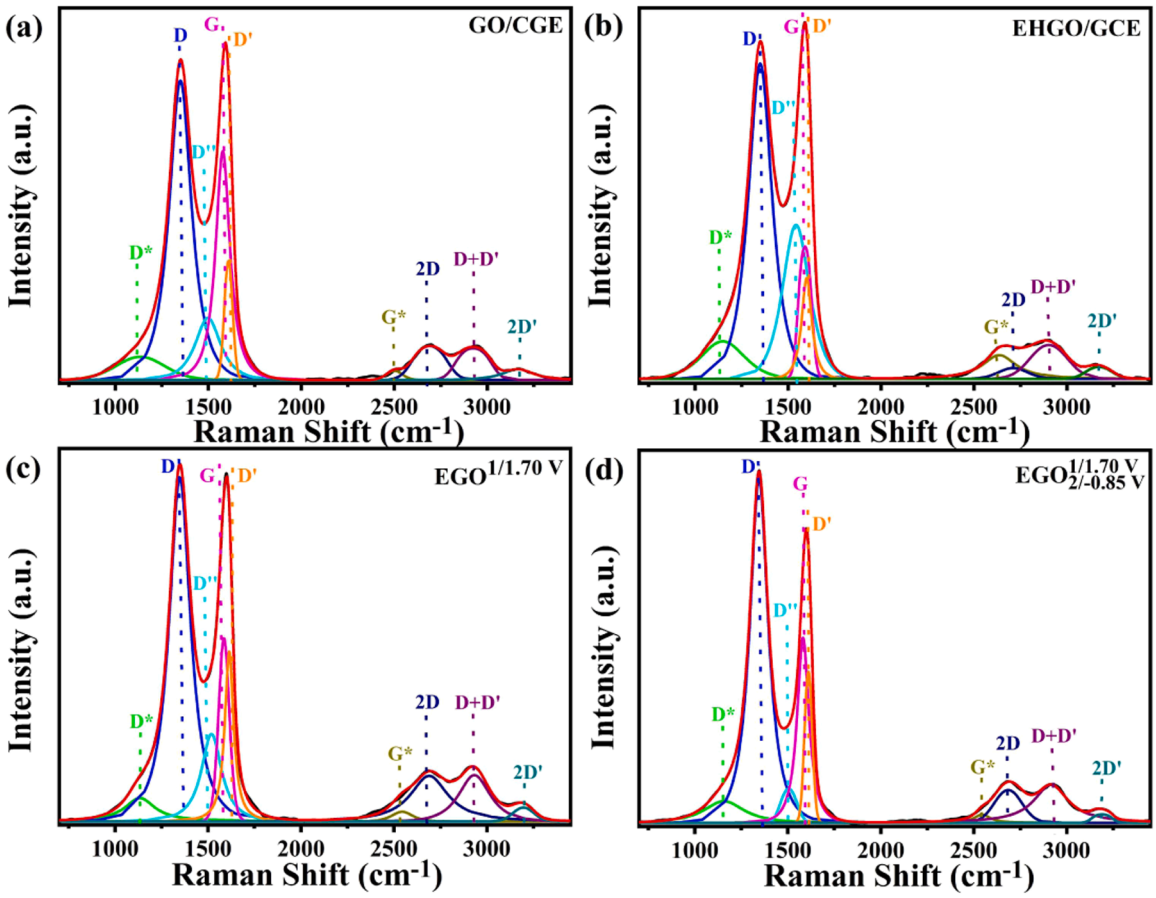

Fig. 2. Deconvolution of the Raman spectra of (a) GO/CGE, (b) EHGO/GCE, (c) $EGO^{1/1.70\ V}$, and (d) $EGO^{1/1.70\ V}_{2/-0.85\ V}$.

vibrations in the hexagonal lattice of sp^2-bonded carbon atoms [47]. Additionally, a peak between the D and G peaks, at around 1498–1543 cm^{-1}, referred to as the D″ band, is indicative of amorphous phases of graphene. Research has confirmed that the defect density of carbon materials can be determined by evaluating the intensity ratios of the D and G bands (I_D/I_G). An increase in the I_D/I_G ratio indicates an increase in the defect density within the carbon structure [48]. The I_D/I_G values were calculated as 1.31, 2.38, 1.88, and 1.86 for GO/CGE, EHGO/GCE, $EGO^{1/1.70\ V}$, and $EGO^{1/1.70\ V}_{2/-0.85\ V}$, respectively (**Table S4**). Notably, the I_D/I_G ratio in EHGO/GCE demonstrates a substantial increase from 1.31 to 2.38 compared to GO/CGE, signifying the emergence of numerous defects on the EHGO/GCE surface. Moreover, the I_{D^*}/I_G ratio escalates with an increase in the oxygen content in the graphite material [49]. The I_{D^*}/I_G ratio of EHGO/GCE is recorded as 0.28, exhibiting the highest value among them, indicative of a higher level of oxygen content in EHGO/GCE.

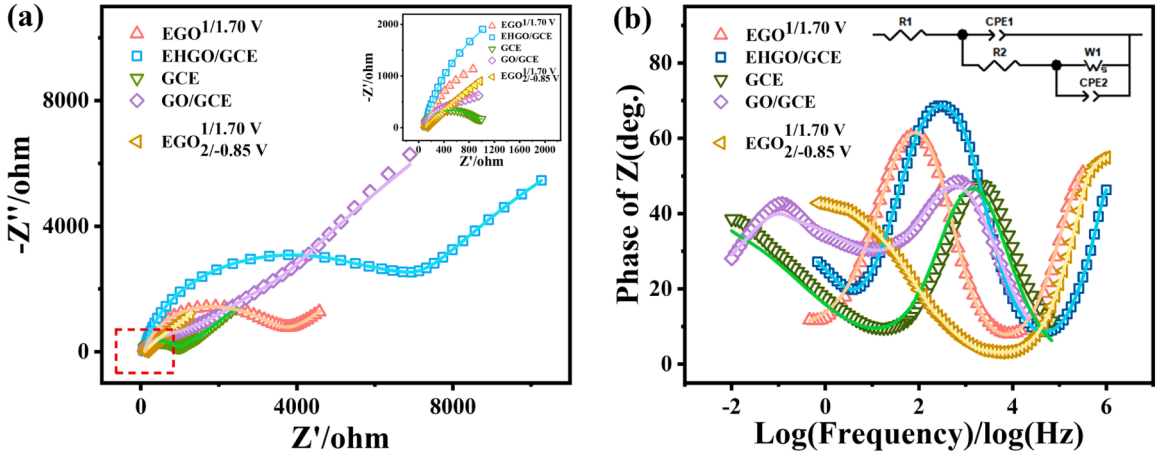

Fig. 3. (a) Nyquist diagrams of EHGO/GCE, $EGO^{1/1.70\ V}$, $EGO^{1/1.70\ V}_{2/-0.85\ V}$, GO/GCE and GCE in 0.1 M KCl solution in the presence of 5 mM $Fe(CN)_6^{3-}/Fe(CN)_6^{4-}$. Inset: The amplified Nyquist diagrams. (b) The corresponding Bode plots. Inset: The electrical equivalent circuit for EHGO/GCE, $EGO^{1/1.70\ V}$, $EGO^{1/1.70\ V}_{2/-0.85\ V}$, and GO/GCE. The symbols and solid lines present the experimental and the fitted data, respectively. The frequency range of EIS was from 1 MHz to 0.1 Hz at 0 .25V.

EIS is also employed for characterizing the interface electrical properties of electrodes. Fig. 3a presents the Nyquist diagrams of EHGO/GCE, $EGO^{1/1.70\ V}$, and $EGO^{1/1.70\ V}_{2/-0.85\ V}$ in 0.1 M KCl solution containing 5 mM $Fe(CN)_6^{3-}/Fe(CN)_6^{4-}$. The corresponding Bode diagrams and electrical equivalent circuit are shown in Fig. 3b. The fitting results were obtained by Z-view software. As depicted in Fig. 3, solid lines represent the fitting curves, while symbols denote experimental data. R1 denotes electrolyte resistance, and R2 represents charge transfer resistance on the electrode surface [50]. W1-R represents the resistance component of the Warburg impedance, indicating mass transport limitations; W1-T is the time constant associated with Warburg impedance, reflecting the rate of mass transport; and W1-P is the phase angle of the Warburg impedance, providing insights into the phase relationship during mass transport processes. CPE1-T and CPE2-T are time constants related to the Constant Phase Element (CPE), indicating the frequency dependence of the capacitive behavior, while CPE1-P and CPE2-P are phase angles that describe the deviation from ideal capacitance in the electrochemical system. **Table S-5** summarizes the fitted parameter values for different electrodes. It can be seen that the charge transfer resistance values (R2) of electrodes followed the order: EHGO/GCE>GO/GCE>GCE>$EGO^{1/1.70\ V}$>$EGO^{1/1.70\ V}_{2/-0.85\ V}$. The results indicated that the electrical conductivity of $EGO^{1/1.70\ V}$ was higher than that of EHGO/GCE. Furthermore, after $EGO^{1/1.70\ V}$ underwent electrochemical reduction, $EGO^{1/1.70\ V}_{2/-0.85\ V}$ showed the best electrical conductivity and electron transfer ability. W1-R is linked to the constraints in mass transport at the electrode interface. Lower values of W1-R signify more efficient mass transport, implying a reduced barrier to the diffusion of species towards and away from the electrode surface. In comparison to other electrodes, EHGO exhibits the highest W1-R, indicating that it has the least efficient mass transport. In addition, the largest CPE1-T value for EHGO/GCE suggests that this electrode has a more significant frequency dispersion in its capacitive behavior compared to the other electrodes. This indicates a less ideal capacitive response, possibly due to surface roughness or porosity at the electrode interface, which affects the charge storage and transfer processes.

3.2. Electrochemical oxidation of UA, DA, and AA

In order to enhance the electrochemical performances of the prepared electrodes, several experimental parameters were optimized for the electro-oxidation of UA, DA, and AA. These parameters included the utilization of different mediums such as 0.1 M NaOH and H_2SO_4, as well as the variation of pH values (ranging from 4.0 to 8.0) in 0.1 M PBS. Moreover, various reduction potentials and oxidation potentials were explored during the optimization process. It was found that the GCE and GO/GCE after undergoing electrochemical treatment in 0.1 M NaOH and H_2SO_4 showed overlapped oxidation peaks for UA, DA, and AA (**Fig. S9 and Fig. S10**). Additionally, it was noted that fragments detached from the GO/GCE during the experiment, particularly when treated with NaOH. However, when the GCE and GO/GCE were electrochemically oxidized in 0.1 M PBS with pH values ranging from 4.0 to 8.0, three distinct and well-defined oxidation peaks for AA, DA, and UA were observed at $EGO^{1/1.70\ V}$, EHGO/GCE, and $EGO^{1/1.70\ V}_{2/-0.85\ V}$ (**Fig. S11**). Therefore, the electrodes underwent electrochemical oxidation treatment in PBS, and the optimized pH value of PBS was found to be 7.0. Additional crucial factors were examined in the treatment of electrodes for the electrochemical response of three compounds, specifically their oxidation potential (**Fig. S12**), reduction potential (**Fig. S13**), and buffer pH (**Fig. S14**). The results showed that the optimized conditions for UA, DA, and AA electro-oxidation were a oxidation potential of 1.70 V, a reduction potential of −0.85 V, and a solution pH of 7.0.

Fig. 4 shows the CVs of bare GCE, GO/GCE, EHGO/GCE, $EGO^{1/1.70\ V}$, and $EGO^{1/1.70\ V}_{2/-0.85\ V}$ in PBS (pH = 7.0) containing 20 μM UA, 20 μM DA, and 500 μM AA, respectively. Bare GCE only presented one broad oxidation peak at a potential of 0.291 V, where the oxidation peaks for AA, DA, and UA were indistinguishable and overlapped, indicating the poor selectivity of bare GCE. In contrast, the GO/GCE showed no oxidation peaks and exhibited a weak current response due to GO's poor electrical conductivity. After electrochemical oxidation, the EHGO/GCE exhibited distinct and separate oxidation peaks for AA, DA, and UA at potentials of 0.017 V, 0.185 V, and 0.326 V, respectively. This separation and clarity in peaks could be attributed to the numerous active defect sites on the EHGO/GCE surface, enhancing electrocatalytic oxidation for these analytes. Similarly, $EGO^{1/1.70\ V}$ showed three well-defined oxidation peaks for AA, DA, and UA at 0.041 V, 0.182 V, and 0.331 V, respectively. The peak currents at $EGO^{1/1.70\ V}$ were higher than those at EHGO/GCE, which could be attributed to the presence of oxo-functional groups and graphene-like structures on the surface of $EGO^{1/1.70\ V}$. Although the $EGO^{1/1.70\ V}_{2/-0.85\ V}$ also displayed three separated oxidation peaks for AA, DA, and UA and 0.003, 0.188, and 0.318 V, the background currents of the electrode increased greatly. Furthermore, the oxidation peak for AA at $EGO^{1/1.70\ V}_{2/-0.85\ V}$ exhibited a lower potential and a little higher peak current compared to the other electrodes. Additionally, EHGO/GCE, $EGO^{1/1.70\ V}$, and $EGO^{1/1.70\ V}_{2/-0.85\ V}$exhibited a pair of redox peaks for DA, indicative of the two-electron oxidation process of DA into reactive dopamine quinones and the subsequent reduction back into DA [51]. In conclusion, these results confirm that EHGO/GCE, $EGO^{1/1.70\ V}$, and $EGO^{1/1.70\ V}_{2/-0.85\ V}$ can simultaneously detect AA, DA, and UA with excellent selectivity.

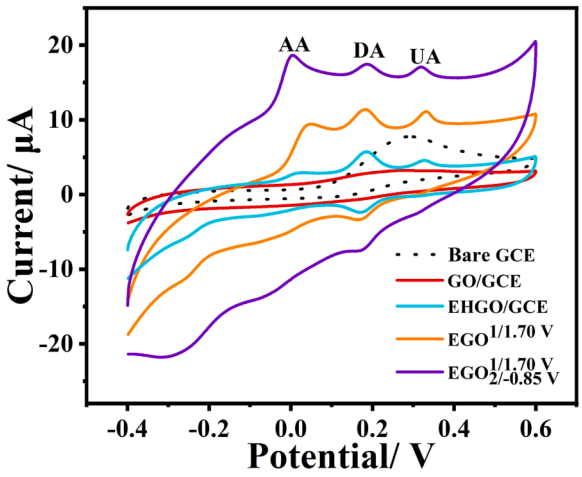

Fig. 4. CVs of bare GCE, GO/GCE, EHGO/GCE, $EGO^{1/1.70\ V}$, and $EGO^{1/1.70\ V}_{2/-0.85\ V}$ in PBS (pH = 7.0) containing 20 μM UA, 20 μM DA, and 500 μM AA at a scan rate of 50 mV s^{-1}, respectively.

3.3. Individual and simultaneous determination of AA, DA, and UA

Under optimized conditions, the individual determination of UA, DA, and AA in a 0.1 M PBS (pH=7.0) was performed by DPV technique at EHGO/GCE, $EGO^{1/1.70\ V}$, and $EGO^{1/1.70\ V}_{2/-0.85\ V}$, respectively. Each substance was detected individually in the presence of the other two, demonstrating the selective capabilities of the electrodes. Fig. 5 shows the DPV curves of EHGO/GCE and the corresponding linear calibration plots for UA, DA, and AA, where the concentration of one analyte increases while the other two remain constant. Specifically, Fig. 5a shows the DPV curves with varying concentrations of UA in the presence of 10 μM DA and 500 μM AA. It was observed that the oxidation peak current of UA increased linearly with its concentration, while the peak currents of AA and DA exhibited some fluctuations, which indicate a certain level of interference from these substances in the determination of UA. This interference is further evidenced by the degraded analytical performance observed in subsequent simultaneous determination

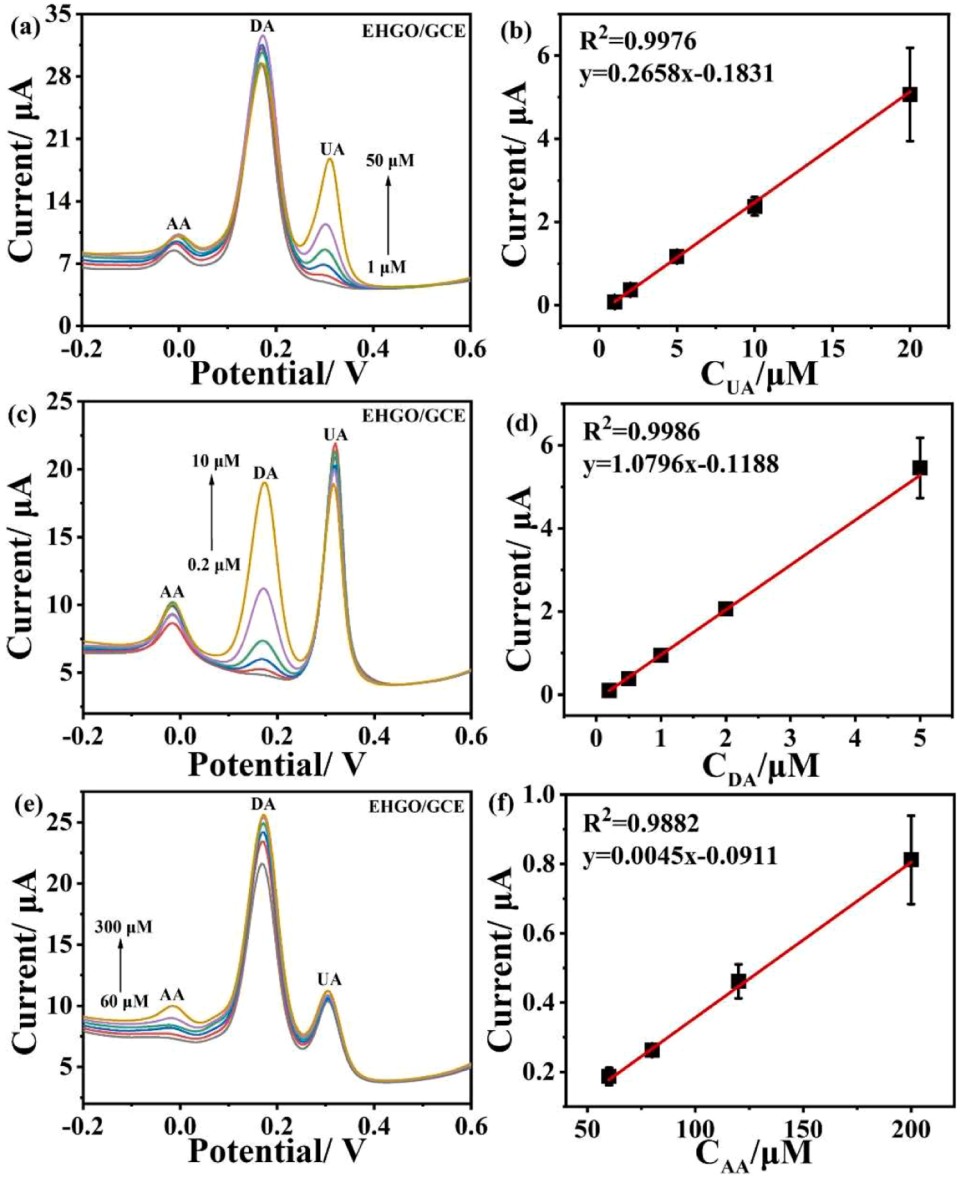

Fig. 5. DPV curves of EHGO/GCE in 0.1 M PBS (pH 7.0) under varied analyte concentrations. Specifically, panels (a), (c), and (e) depict changes in one analyte's concentration while the other two remain fixed: (a) UA ranges from 1 μM to 50 μM with DA at 10 μM and AA at 500 μM; (c) DA ranges from 0.2 μM to 10 μM, with UA at 20 μM and AA at 500 μM; (e) AA ranges from 60 μM to 300 μM, with UA at 20 μM and DA at 10 μM. Panels (b), (d), and (f) provide the linear calibration plots, correlating peak current with the concentrations of UA, DA, and AA, respectively.

experiments. Fig. 5b, d, **and** f demonstrate that the oxidation peak currents for UA, DA, and AA at EHGO/GCE exhibit a linear relationship with increasing concentrations within the ranges of 1–20 μM for UA, 0.2–5 μM for DA, and 60–200 μM for AA, respectively. The detection limits were determined to be 1 μM for AA, 0.2 μM for DA, and 60 μM for UA, highlighting the excellent selectivity and potential for quantitative analysis using EHGO/GCE.

Figs. 6 and 7 display the DPV curves of $EGO^{1/1.70\ V}$ and $EGO^{1/1.70\ V}_{2/-0.85\ V}$ for the determination of UA, DA, and AA. Consistent with our previous observations, we also noted variations in the peaks of the other two interfering substances, suggesting their impact on the analytical process. The linear ranges, detection limits, and sensitivities for the individual determination of UA, DA, and AA at EHGO/GCE, $EGO^{1/1.70\ V}$, and $EGO^{1/1.70\ V}_{2/-0.85\ V}$ are summarized in **Table S6**. The sensitivity of the electrodes for determining these analytes showed that $EGO^{1/1.70\ V}_{2/-0.85\ V}$ had the highest sensitivity, followed by $EGO^{1/1.70\ V}$, and then EHGO/GCE. However, $EGO^{1/1.70\ V}_{2/-0.85\ V}$ also exhibited higher background noise and a higher detection limit for DA, which may affect its practical applicability for low concentration measurements. Moreover, simultaneous determination of these analytes was also conducted at EHGO/GCE, $EGO^{1/1.70\ V}$, and $EGO^{1/1.70\ V}_{2/-0.85\ V}$, as shown in **Figures S15–17 and Table S7**, which revealed well-defined oxidation peaks for UA, DA, and AA that increased linearly with the concentrations of the analytes. **Table S8** compares these findings with other electrodes documented in the literature, underscoring the superior analytical performance of these electrodes for selective and sensitive determination of UA, DA, and AA. These results confirm the feasibility of simultaneously determining these three analytes in a mixed solution using the specified electrodes. It has been observed that not only does the peak for a specific analyte increase linearly with its added concentration, but the peaks for other analytes, maintained at constant concentrations, also undergo changes. This phenomenon may be attributed to molecular interactions that alter the electrochemical behavior of these compounds. Such interactions could

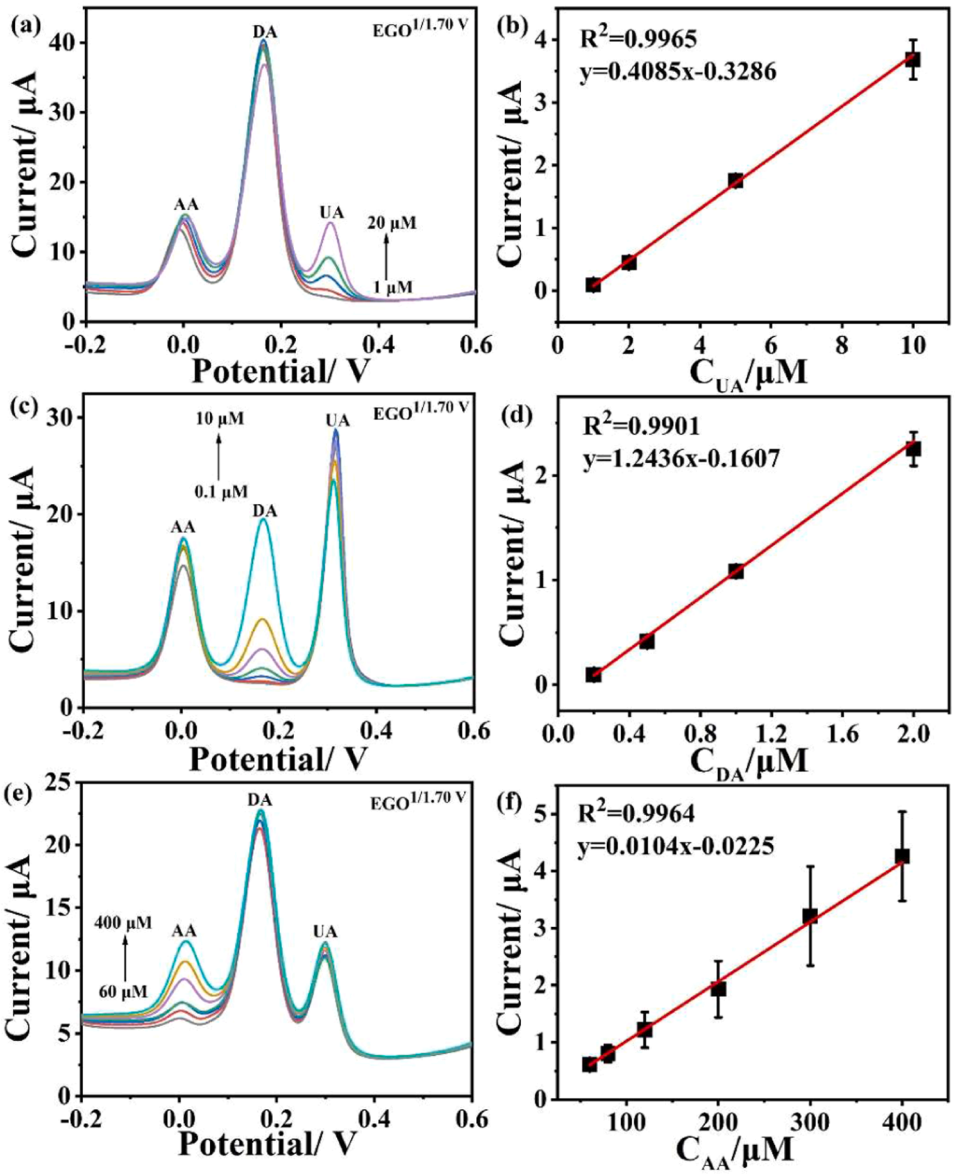

Fig. 6. DPV curves of $EGO^{1/1.70\ V}$ under varied analyte concentrations. Other experimental conditions are the same as in Figure 5.

modify the effective free concentration of the fixed compounds available for electrochemical reactions, thereby impacting their peak currents. Furthermore, these compounds might compete for identical adsorption sites on the electrode surface. An increase in the concentration of one analyte could disrupt the surface other interfering substances, subsequently affecting their peak currents. Additionally, the diffusion of the analyte to the electrode surface could perturb the diffusion layer composition, which in turn influences the mass transport of other compounds to the electrode and affects their peak currents.

The expected concentration ranges for DA, UA, and AA in biological samples are essential for assessing the applicability of sensors. DA, a neurotransmitter, is present in the brain and is crucial for regulating the central nervous system. Its abnormal levels can lead to neurological disorders like Parkinson's disease and schizophrenia. The concentration of DA in the brain can vary, but typical physiological levels are in the nanomolar to low micromolar range [52]. UA, the main end product of purine metabolism, is typically found in the range of 150–400 μM in human blood plasma [53]. High concentrations can lead to conditions such as gout and hyperuricemia. AA, an essential component in human diet and a popular antioxidant, is commonly found in the range of 50–150 μM in plasma, and its levels can be lower in tissues and other body fluids [54]. Considering the concentration ranges of these three substances within biological samples and the linear detection range of our method, it is evident that our sensing approach holds potential for the detection of biological samples.

3.4. Antifouling performances

To evaluate the resistance to chemical fouling of various electrodes, Fig. 8 shows the successive measurements conducted on EHGO/GCE, $EGO^{1/1.70\ V}$, and $EGO^{1/1.70\ V}_{2/-0.85\ V}$ in 0.1 M PBS at pH 7.0 in the presence of 5 μM UA, 1 μM DA, and 120 μM AA. The corresponding normalized peak current percentages are also shown. For the EHGO/GCE, an increasing trend in the oxidation peak currents of UA, DA, and AA was observed across successive measurements. This instability might be attributed to the abundant active sites and defects that are prone to change. Three distinct oxidation peaks were noted for UA, DA, and AA at potentials of 0.292 V, 0.164 V, and −0.024 V, respectively. Here, the oxidation peak currents of DA and AA increased progressively with additional measurements, while the peak current for UA slightly decreased. However,

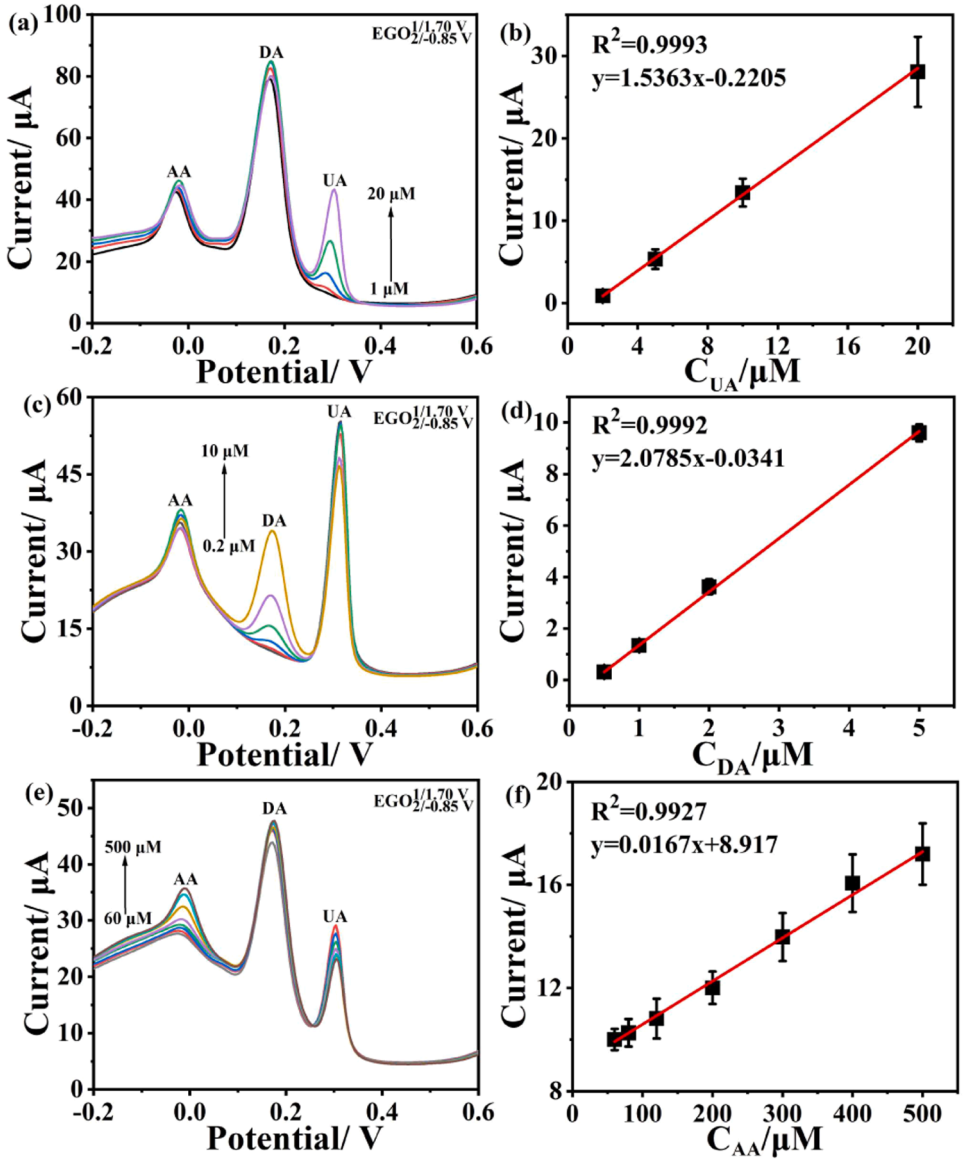

Fig. 7. DPV curves of $EGO^{1/1.70\ V}_{2/-0.85\ V}$ under varied analyte concentrations. Other experimental conditions are the same as in Fig. 5.

by the tenth measurement, the UA peak current remained approximately 84 % of its initial value. Conversely, after electrochemical reduction, the $EGO^{1/1.70\ V}_{2/-0.85\ V}$ exhibited significant fouling by oxidation products. The peak currents for UA and DA in the second measurement dropped sharply to about 70 % and 44 % of their first scan values, respectively, highlighting severe fouling after the initial electrochemical oxidation in PBS. **Fig. S18** shows the DPV responses of EHGO/GCE, $EGO^{1/1.70\ V}$, and $EGO^{1/1.70\ V}_{2/-0.85\ V}$ in pure PBS solution. Notably, $EGO^{1/1.70\ V}_{2/-0.85\ V}$ showed a broad oxidation peak around 0 V, likely reflecting background noise attributed to the oxidation of quinoidal-like functionalities on the electrode surface [55]. Although the oxidation peak currents of AA remained almost stable during continuous measurements for $EGO^{1/1.70\ V}_{2/-0.85\ V}$, the electro-oxidation of UA was affected by the background peak. These results affirm that both EHGO/GCE and $EGO^{1/1.70\ V}$ exhibit high electrocatalytic activity and excellent selectivity for the oxidation of UA, DA, and AA, along with robust resistance to fouling by their oxidation products.

The electro-oxidation of UA produces a diimine species that exhibits strong adsorption on the electrode surface, leading to chemical fouling of the electrode. We investigated the adsorption behavior of diimine species on different electrodes (**Fig. S19**). For EHGO/GCE and $EGO_{1/1.70\ V}$, a clear UA oxidation peak was observed during the anodic scan starting from 0V. In the reverse scan, a small oxidation peak I_c appeared, corresponding to the reduction peak of adsorbed diimine species. Further negative scanning led to a large reduction peak, indicating the reduction of oxo-functional groups. However, during the second scan, the Ic peak became more pronounced, attributed to the reduction in oxo-functional groups on the electrode surface, resulting in increased adsorption of diimine species. Additionally, an II_c peak appeared that also derived from the reduction of adsorbed species. Conversely, for $EGO^{1/1.70\ V}_{2/-0.85\ V}$, the results of the two scans were consistent, with both reduction peaks being relatively prominent. This suggests that diimine species are more prone to adsorption on this electrode compared to EHGO/GCE and $EGO_{1/1\ .70V}$.

To assess the anti-biofouling property of various electrodes, we investigated the successive DPV responses of EHGO/GCE, $EGO^{1/1.70\ V}$, and $EGO^{1/1.70\ V}_{2/-0.85\ V}$ in 0.1 M PBS (pH 7.0) with a 1:50 dilution of human serum, containing a mixture of 5 μM UA, 1 μM DA, and 120 μM AA (Fig. 9). Initially, the electrodes were tested with the UA, DA, and AA mixture in PBS without serum for the first three measurements. Upon

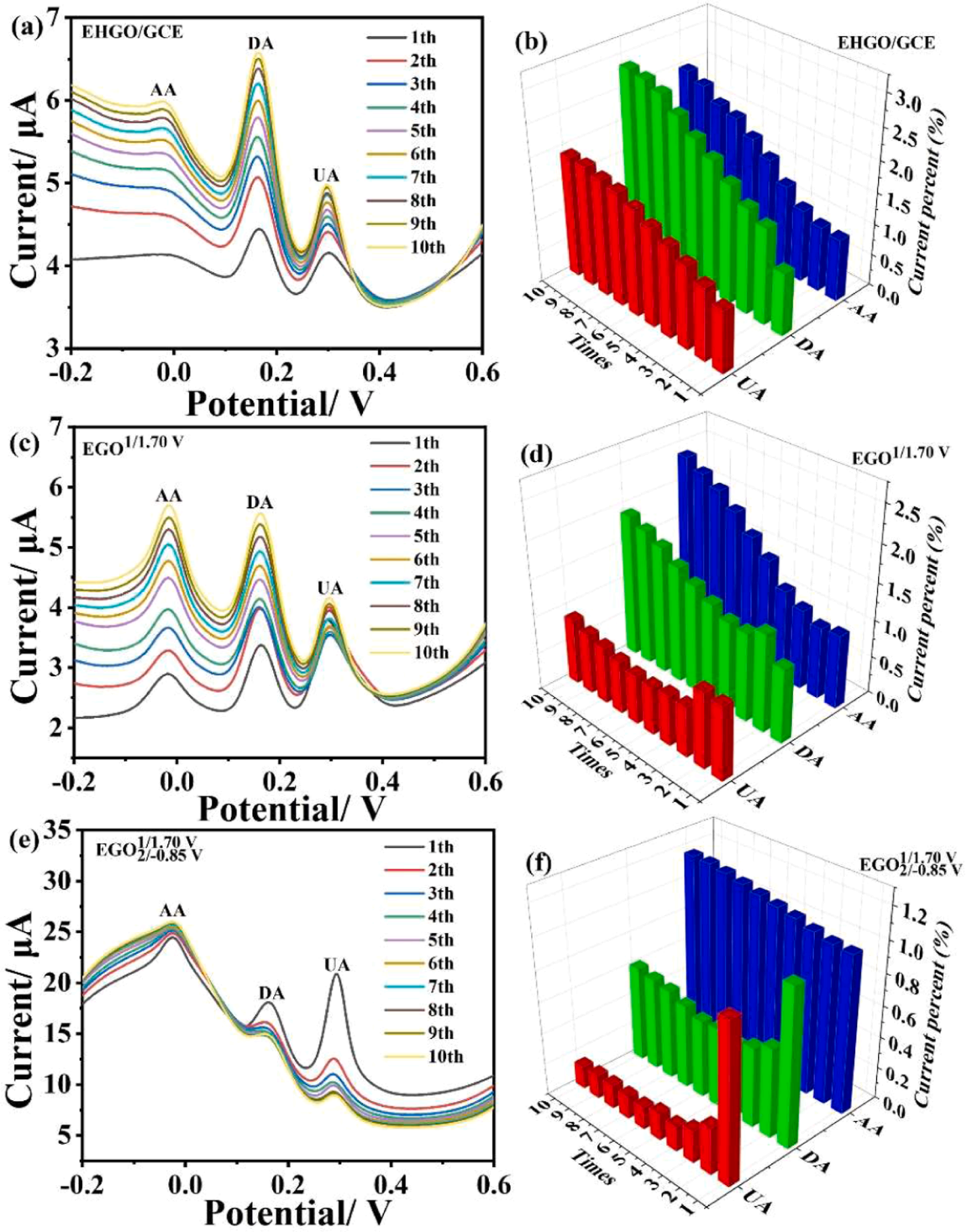

Fig. 8. Successive ten times DPV responses of (a) EHGO/GCE, (c) $EGO^{1/1.70\ V}$, and (e) $EGO^{1/1.70\ V}_{2/-0.85\ V}$ in 0.1 M PBS (pH = 7.0) in the presence of 5 μM UA, 1 μM DA, and 120 μM AA. The corresponding normalized peak current percentages for (b) EHGO/GCE, (d) $EGO^{1/1.70\ V}$, and (f) $EGO^{1/1.70\ V}_{2/-0.85\ V}$.

adding serum, the oxidation peak currents for these analytes increased significantly for EHGO/GCE and $EGO^{1/1.70V}$ compared to the serum-free solution, indicating high sensitivity to the electroactive components in serum. For EHGO/GCE, the oxidation peak currents of UA, DA, and AA initially decreased but then gradually increased in the presence of diluted human serum. At the final measurement, the peak currents for UA, DA, and AA remained at 98 %, 90 %, and 125 % of their initial values, respectively, demonstrating EHGO/GCE's excellent anti-biofouling properties. However, $EGO^{1/1.70\ V}$ showed a consistent decrease in peak currents for UA, DA, and AA across ten tests, attributed to the adsorption of non-specific proteins in human serum causing significant biofouling. Similarly, $EGO^{1/1.70\ V}_{2/-0.85\ V}$ exhibited severe contamination by serum proteins. To further assess biofouling effects, the electrodes were immersed in undiluted human serum for 30 min and tested again with the ternary mixture in 0.1 M PBS (pH 7.0), as shown in **Fig. S20**. Results confirmed that EHGO/GCE maintained good anti-

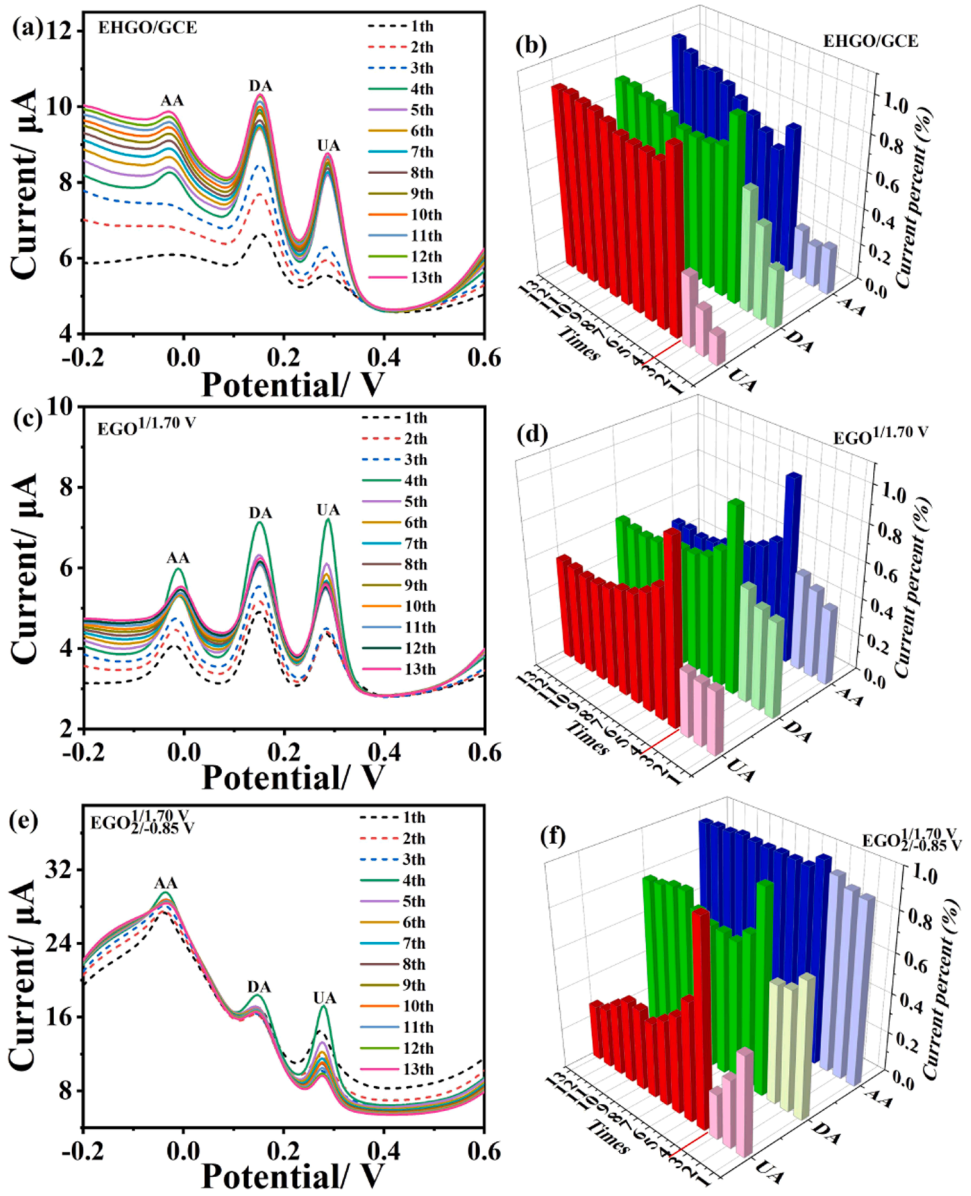

Fig. 9. Successive DPV responses of (a) EHGO/GCE, (c) $EGO^{1/1.70\ V}$, and (e) $EGO^{1/1.70\ V}_{2/-0.85\ V}$ 0.1 M PBS (pH=7.0) containing 5 μM UA, 1 μM DA, and 120 μM AA, shown before (1st-3rd scans, dotted lines) and after (4th-13th scans, solid lines) the addition of diluted human serum (50-fold dilution). The corresponding normalized peak current percentage of (b) EHGO/GCE, (d) $EGO^{1/1.70\ V}$, and (f) $EGO^{1/1.70\ V}_{2/-0.85\ V}$.

biofouling properties, whereas the surfaces of $EGO^{1/1.70\ V}$ and $EGO^{1/1.70\ V}_{2/-0.85\ V}$ were heavily fouled by non-specific proteins. Notably, the oxidation peak current for AA at $EGO^{1/1.70\ V}$ almost disappeared after exposure to undiluted human serum, indicating that its active sites for AA were blocked by biomacromolecules. This suggests that the oxo-functional groups and defect sites on EHGO/GCE's surface play crucial roles in enhancing its anti-biofouling performance.

3.5. Real sample analysis

In order to evaluate the reliability of the prepared sensor for practical application, the EHGO/GCE, $EGO^{1/1.70\ V}$, and $EGO^{1/1.70\ V}_{2/-0.85\ V}$ were investigated for the detection of UA in real human serum samples using a standard addition method by DPV (**Fig. S21**). The serum samples were first diluted 200 times with 0.1 M PBS (pH 7.0) prior to measurement. The results indicated that the determined UA concentration in the serum samples was calculated to be 99 μM, 120 μM, and 136 μM for EHGO/GCE, $EGO^{1/1.70\ V}$, and $EGO^{1/1.70\ V}_{2/-0.85\ V}$, respectively, which were slightly lower than the clinical medicine test result (Enzymatic Assay method,150 μM). Therefore, the proposed sensors exhibit considerable promise for the accurate detection of UA in real human serum samples.

3.6. Electrochemical oxidation mechanism study of GO

Since hoely GO is generated in-situ on the surface of GCE electrodes, it is challenging to directly characterize its porous structure using methods like transmission electron microscopy (TEM). Instead, we can use indirect methods such as electrochemistry to characterize its surface structure. Fig. 10 shows the consecutive CVs of GO/GCE, $GO_{-0.75}$/GCE, and EHGO/GCE in 0.1 M PBS (pH=7.0) under a saturated nitrogen atmosphere. It is noticeable that the initial cycle of the CV curves exhibits some distinctive features. However, from the second cycle onwards, there is minimal variation in the positions of the characteristic peaks. Notably, the peak current diminishes with each cycle for these three

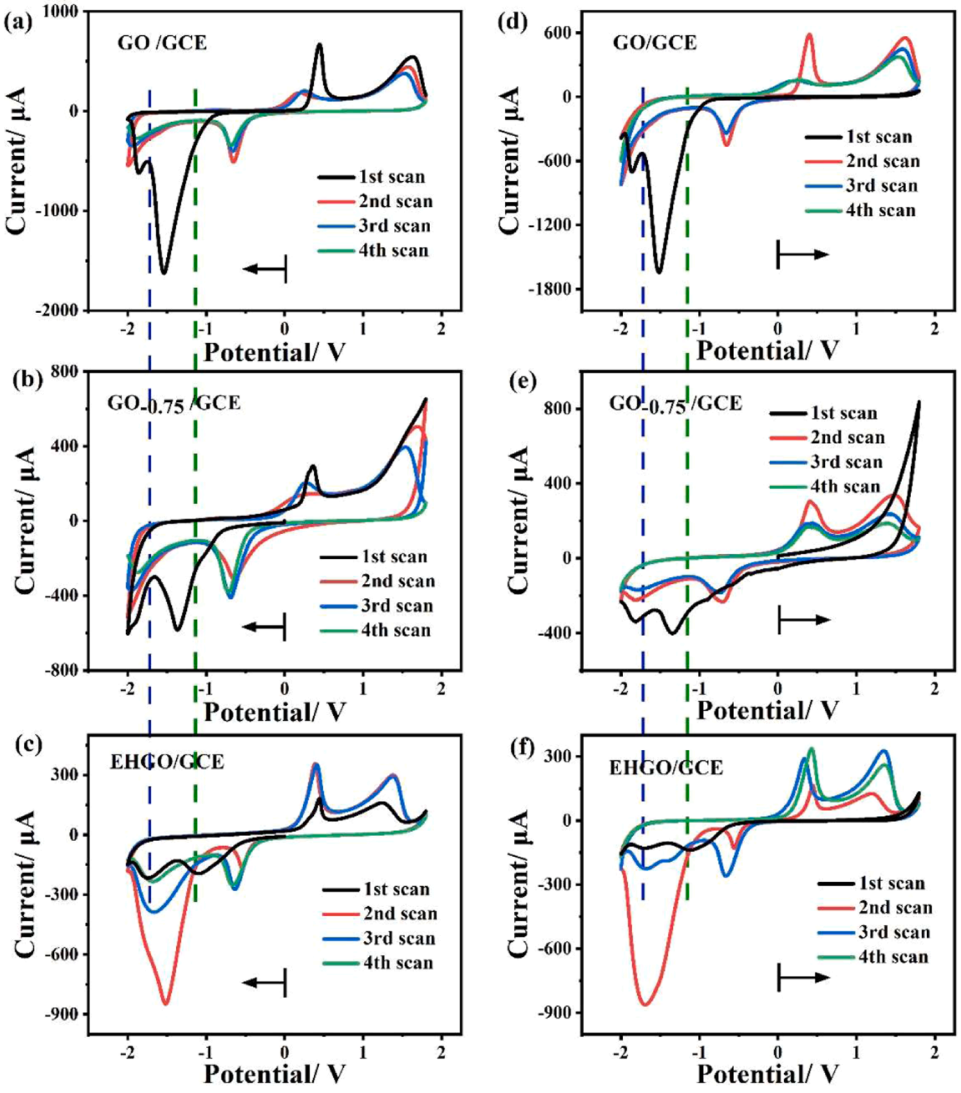

Fig. 10. CVs of (a, d) GO/GCE, (b, e) $GO_{-0.75}$/GCE, and (c, f) EHGO/GCE in 0.1 M PBS (pH = 7.0), under nitrogen saturation, with initial scan conducted in both negative (a, b, and c) and positive (d, e, and f) directions at a scan rate of 50 mV s^{-1}.

electrodes. After 30 scanning segments, the EHGO's peak current is significantly reduced (**Fig. S22**). This decline is due to the prolonged exposure to extreme anodic and cathodic potentials during scanning, resulting in substantial damage to the electrode's surface films (**Fig. S23 and S24**). In the negative scan direction starting from 0 V, the reduction of GO/GCE commenced at −0.80 V during the initial scan, featuring a pronounced reduction peak at approximately −1.54 V and a smaller peak at −1.86 V. These peaks result from the reduction of epoxy and carbonyl groups on the GO surface [56]. During the subsequent oxidation processes, two distinct oxidation waves were observed at 0.2 V and 1.5 V, respectively. In the second scan, the initial reduction peaks at −1.54 V and −1.86 V were absent, replaced by a new reduction wave at −0.65 V. In the case of $GO_{-0.75}$/GCE, the reduction peak showed a significant decrease in current compared to GO/GCE, attributed to the reduced presence of oxo-functional groups through electrochemical reduction. Conversely, the reduction of EHGO/GCE occurred at about −0.3 V, representing a 500 mV potential shift relative to GO/GCE. Additionally, two well-defined reduction peaks at approximately −1.10 V and −1.76 V were observed at EHGO/GCE. This indicates that the reduction of oxo-functional groups on the EHGO surface occurred at a higher potential, which means it required less reducing potential, suggesting enhanced electro-activity. During the second scan, a reduction peak at around −0.65 V was also noted for EHGO/GCE, and notably, the sharp intense reduction peak at −1.54 V persisted, unlike with GO/GCE and $GO_{-0.75}$/GCE. These results demonstrate that EHGO/GCE exhibits distinct electrochemical activity compared to GO/GCE and $GO_{-0.75}$/GCE.

The reduction processes of these electrodes were also examined using DPV, as depicted in **Fig. S25**. DPV offers significantly enhanced resolution capabilities. The DPV curves also revealed that the reduction of certain oxo-functional groups on EHGO/GCE occurred at a more positive potential, indicating a reduced requirement for reducing potential as compared to other electrodes. At high potentials, water oxidizes on the surface of GO, potentially generating hydroxyl radicals. These radicals can quickly react with the functional groups in GO or might even attack its carbon backbone. This interaction can result in the loss of original functional groups or cause structural breaks, ultimately leading to the formation of holes. To demonstrate this, CV scans of GO/GCE electrodes oxidized under different conditions are presented. **Fig. S26** shows CV scans of GO/GCE after oxidation at 1.75 V in a 0.1 M PBS (pH 7.0) solution containing 1 mM 4-Amino-TEMPO. The CV profiles differ significantly between the electrode oxidized in 0.1 M PBS (pH 7.0) containing 1 mM 4-Amino-TEMPO and the electrode oxidized in pure PBS. The little redox peaks were attributed to the immobilization of

TEMPO. The results indicate that in the presence of TEMPO, the anodic potential applied results in the oxidation of the more readily oxidizable TEMPO, rather than water. Consequently, this prevents the formation of pores in the electrode structure, as water oxidation, which typically leads to pore formation, does not occur.

4. Conclusion

Electrochemical methods were employed to in-situ generate materials with graphene-like electrochemical properties on GCE, while EHGO was generated in-situ on GO-modified GCE surfaces. The study explored the simultaneous determination of AA, DA, and UA using these electrodes. The electrocatalytic activity, detection limits, sensitivity, background noise, and anti-fouling properties of different electrodes were thoroughly discussed. Additionally, the formation mechanism of EHGO was investigated. The results demonstrate that the electrochemical in-situ method is an environmentally friendly and simple approach for preparing high-performance electrodes, which shows promising application potential in electroanalysis and electrocatalysis.

CRediT authorship contribution statement

Gang Li: Writing – original draft, Visualization, Investigation. **Ming Qin:** Writing – review & editing, Visualization, Investigation. **Qiang Zhang:** Writing – review & editing, Visualization, Investigation. **Baiqing Yuan:** Writing – review & editing, Writing – original draft, Visualization, Supervision, Funding acquisition, Conceptualization. **Lanxin Xue:** Validation. **Shuning Zhang:** Validation. **Jingfei Yan:** Validation. **Chunying Xu:** Writing – review & editing, Supervision.

Declaration of competing interest

The authors declare that they have no known competing financial interests or personal relationships that could have appeared to influence the work reported in this paper.

Acknowledgments

This research was funded by the National Natural Science Foundation of China (No. 22272068).

Supplementary materials

Supplementary material associated with this article can be found, in the online version, at doi:10.1016/j.cartre.2024.100447.

Data availability

Data will be made available on request.

References

[1] Z. Wang, M. Li, B. Zhang, Y. Ye, T. Yang, H. Zeng, X. Luo, Enhanced long-term antifouling ability and enrichment effect of a vertically ordered mesoporous silica film via covalent linkage of chondroitin sulfate for in-situ detection of Cu^{2+} in real environmental samples, ACS. ES. T. Water. 3 (8) (2023) 2108–2119.
[2] G. Archbold, C. Parra, H. Carrillo, A.M. Mouazen, Towards the implementation of isfet sensors for in-situ and real-time chemical analyses in soils: a practical review, Comput. Electron. Agric. 209 (2023) 107828.
[3] J. Sun, Z. Wang, J. Guan, Single-atom nanozyme-based electrochemical sensors for health and food safety monitoring, Food Chem. (2023) 136518.
[4] Q. Du, W. Wang, X. Zeng, X. Luo, Antifouling zwitterionic peptide hydrogel based electrochemical biosensor for reliable detection of prostate specific antigen in human serum, Anal. Chim. Acta 1239 (2023) 340674.
[5] W. Zhang, R. Wang, F. Luo, P. Wang, Z. Lin, Miniaturized electrochemical sensors and their point-of-care applications, Chin. Chem. Lett. 31 (3) (2020) 589–600.
[6] L. Karadurmus, S.I. Kaya, A. Cetinkaya, S.A. Ozkan, New brand MXene-based electrochemical point-of-care sensors as novel diagnostic devices, Trac-Trends Anal. Chem. (2023) 117145.
[7] S.S. Soliman, A.M. Mahmoud, M.R. Elghobashy, H.E. Zaazaa, G.A. Sedik, Point-of-care electrochemical sensor for selective determination of date rape drug "ketamine" based on core-shell molecularly imprinted polymer, Talanta 254 (2023) 124151.
[8] J.J. Gooding, Finally, a simple solution to biofouling, Nat. Nanotechnol. 14 (12) (2019) 1089–1090.
[9] X. Qiao, Y. Cai, Z. Kong, Z. Xu, X. Luo, A wearable electrochemical sensor based on anti-fouling and self-healing polypeptide complex hydrogels for sweat monitoring, ACS. Sens. 8 (7) (2023) 2834–2842.
[10] X. Zhu, L. Xuan, J. Gong, J. Liu, X. Wang, F. Xi, J. Chen, Three-dimensional macroscopic graphene supported vertically-ordered mesoporous silica-nanochannel film for direct and ultrasensitive detection of uric acid in serum, Talanta 238 (2022) 123027.
[11] Y. Zhang, L. Zhang, C. Li, J. Han, W. Huang, J. Zhou, Y. Yang, Hydrophilic antifouling 3D porous MXene/holey graphene nanocomposites for electrochemical determination of dopamine, Microchem. J. 181 (2022) 107713.
[12] D. Deng, K. Novoselov, Q. Fu, N. Zheng, Z. Tian, X. Bao, Catalysis with two-dimensional materials and their heterostructures, Nat. Nanotechnol. 11 (3) (2016) 218–230.
[13] H. Huang, H. Shi, P. Das, J. Qin, Y. Li, X. Wang, F. Su, P. Wen, S. Li, P. Lu, The chemistry and promising applications of graphene and porous graphene materials, Adv. Funct. Mater. 30 (41) (2020) 1909035.
[14] S. Wu, Q. He, C. Tan, Y. Wang, H. Zhang, Graphene-based electrochemical sensors, Small. 9 (8) (2013) 1160–1172.
[15] S. Pattnaik, K. Swain, Z. Lin, Graphene and graphene-based nanocomposites: biomedical applications and biosafety, J. Mater. Chem. B. 4 (48) (2016) 7813–7831.
[16] S. Patil, C. Rajkuberan, S. Sagadevan, Recent biomedical advancements in graphene oxide and future perspectives, J. Drug Delivery Sci. Technol. (2023) 104737.
[17] G. Li, C. Xu, H. Xu, L. Gan, K. Sun, B. Yuan, Tunable graphene oxide for the low-fouling electrochemical sensing of uric acid in human serum, Analyst 148 (11) (2023) 2553–2563.
[18] C. Galande, W. Gao, A. Mathkar, A.M. Dattelbaum, T.N. Narayanan, A.D. Mohite, P.M. Ajayan, Sci. Eng. Graphene Oxide Part. Part. Syst. Charact. 31 (6) (2014) 619–638.
[19] P. Brisebois, M. Siaj, Harvesting graphene oxide–years 1859 to 2019: a review of its structure, synthesis, properties and exfoliation, J. Mater. Chem. C. 8 (5) (2020) 1517–1547.
[20] Y.Y. Khine, X. Wen, X. Jin, T. Foller, R. Joshi, Functional groups in graphene oxide, Phys. Chem. Chem. Phys. 24 (43) (2022) 26337–26355.
[21] Y. Qiu, S. Moore, R. Hurt, I. Külaots, Influence of external heating rate on the structure and porosity of thermally exfoliated graphite oxide, Carbon. N. Y. 111 (2017) 651–657.
[22] V. Agarwal, P.B. Zetterlund, Strategies for reduction of graphene oxide–a comprehensive review, Chem. Eng. J. 405 (2021) 127018.
[23] R. Jakhar, J.E. Yap, R. Joshi, Microwave reduction of graphene oxide, Carbon. N. Y. 170 (2020) 277–293.
[24] W. Liu, G. Speranza, Tuning the oxygen content of reduced graphene oxide and effects on its properties, ACS. Omega 6 (9) (2021) 6195–6205.
[25] A. Zakaria, E.S. Vasquez, K.B. Walters, D. Leszczynska, Functional holey graphene oxide: a new electrochemically transformed substrate material for dopamine sensing, in: RSC. Adv., 5, 2015, pp. 107123–107135.
[26] G.P. Kotchey, B.L. Allen, H. Vedala, N. Yanamala, A.A. Kapralov, Y.Y. Tyurina, J. Klein-Seetharaman, V.E. Kagan, A. Star, The enzymatic oxidation of graphene oxide, ACS. Nano 5 (3) (2011) 2098–2108.
[27] G. Li, C. Xu, H. Xu, L. Gan, K. Sun, B. Yuan, Tunable graphene oxide for the low-fouling electrochemical sensing of uric acid in human serum, Analyst 148 (11) (2023) 2553–2563.
[28] L. Xuan, W. Liao, M. Wang, H. Zhou, Y. Ding, F. Yan, J. Liu, H. Tang, F. Xi, Integration of vertically-ordered mesoporous silica-nanochannel film with electro-activated glassy carbon electrode for improved electroanalysis in complex samples, Talanta 225 (2021) 122066.
[29] R. Su, H. Tang, F. Xi, Sensitive electrochemical detection of p-nitrophenol by pre-activated glassy carbon electrode integrated with silica nanochannel array film, Front. Chem. 10 (2022) 954748.
[30] L. Huang, R. Su, F. Xi, Sensitive detection of noradrenaline in human whole blood based on Au nanoparticles embedded vertically-ordered silica nanochannels modified pre-activated glassy carbon electrodes, Front. Chem. 11 (2023) 1126213.
[31] M. Santhiago, C.M. Maroneze, C.C. Silva, M.N. Camargo, L.T. Kubota, Electrochemical oxidation of glassy carbon provides similar electrochemical response as graphene oxide prepared by tour or hummers routes, ChemElectroChem. 2 (5) (2015) 761–767.
[32] C. Xu, G. Li, L. Gan, B. Yuan, In-situ electrochemical formation of oxo-functionalized graphene on glassy carbon electrode with chemical fouling recovery and antibiofouling properties for electrochemical sensing of reduced glutathione, Antioxidants 12 (1) (2022) 8.
[33] Q. Wei, S. Pei, G. Wen, K. Huang, Z. Wu, Z. Liu, W. Ma, H.-M. Cheng, W. Ren, High yield controlled synthesis of nano-graphene oxide by water electrolytic oxidation of glassy carbon for metal-free catalysis, ACS. Nano 13 (8) (2019) 9482–9490.
[34] M. Qin, J. Zhu, J. Zhao, B. Yuan, S. Liu, T. Cai, C. Xu, Anodic and cathodic dual-mode cysteine detection utilizing a glassy carbon electrode co-activated by electrochemical pretreatment and fully fluorinated cobalt phthalocyanine, J. Electroanal. Chem. 977 (2025) 118861.

[35] H. Park, S.K. Terhorst, R.K. Bera, R. Ryoo, Template dissolution with NaOH–HCl in the synthesis of zeolite-templated carbons: effects on oxygen functionalization and electrical energy storage characteristics, Carbon. N. Y. 155 (2019) 570–579.
[36] G. Reina, C. Gabellini, M. Maranska, F. Grote, S.M. Chin, L. Jacquemin, F. Berger, P. Posocco, S. Eigler, A. Bianco, The importance of molecular structure and functionalization of oxo-graphene sheets for gene silencing, Carbon. N. Y. 195 (2022) 69–79.
[37] Y. Wang, F. Grote, Q. Cao, S. Eigler, Regiochemically oxo-functionalized graphene, guided by defect sites, as catalyst for oxygen reduction to hydrogen peroxide, J. Phys. Chem. Lett. 12 (2021) 10009–10014.
[38] A. Dekanski, J. Stevanović, R. Stevanović, B.Ž. Nikolić, V.M. Jovanović, Glassy carbon electrodes: I. characterization and electrochemical activation, Carbon. N. Y. 39 (8) (2001) 1195–1205.
[39] G. Li, C. Xu, H. Xu, L. Gan, K. Sun, B. Yuan, Tunable graphene oxide for the low-fouling electrochemical sensing of uric acid in human serum, Analyst 148 (11) (2023) 2553–2563.
[40] J.A. Quezada-Renteria, C.O. Ania, L.F. Chazaro-Ruiz, J.R. Rangel-Mendez, Influence of protons on reduction degree and defect formation in electrochemically reduced graphene oxide, Carbon. N. Y. 149 (2019) 722–732.
[41] S.Y. Toh, K.S. Loh, S.K. Kamarudin, W.R.W. Daud, Graphene production via electrochemical reduction of graphene oxide: synthesis and characterisation, Chem. Eng. J. 251 (2014) 422–434.
[42] P. Yang, Q. Liu, J. Liu, H. Zhang, Z. Li, R. Li, L. Liu, J. Wang, Bovine serum albumin-coated graphene oxide for effective adsorption of uranium (VI) from aqueous solutions, Ind. Eng. Chem. Res. 56 (13) (2017) 3588–3598.
[43] J. Cheng, Y. Qiu, R. Huang, W. Yang, J. Zhou, K. Cen, Biodiesel production from wet microalgae by using graphene oxide as solid acid catalyst, Bioresour. Technol. 221 (2016) 344–349.
[44] A. Puziy, O. Poddubnaya, R. Socha, J. Gurgul, M. Wisniewski, XPS and NMR studies of phosphoric acid activated carbons, Carbon. N. Y. 46 (15) (2008) 2113–2123.
[45] H.Muckenhuber Sadezky, H. Grothe, R. Niessner, U. Pöschl, Raman microspectroscopy of soot and related carbonaceous materials: spectral analysis and structural information, Carbon. N. Y. 43 (8) (2005) 1731–1742.
[46] K. Krishnamoorthy, M. Veerapandian, K. Yun, S.-J. Kim, The chemical and structural analysis of graphene oxide with different degrees of oxidation, Carbon. N. Y. 53 (2013) 38–49.
[47] N. Liu, F. Luo, H. Wu, Y. Liu, C. Zhang, J. Chen, One-step ionic-liquid-assisted electrochemical synthesis of ionic-liquid-functionalized graphene sheets directly from graphite, Adv. Funct. Mater. 18 (10) (2008) 1518–1525.
[48] M. Alanyalıoğlu, J.J. Segura, J. Oro-Sole, N. Casañ-Pastor, The synthesis of graphene sheets with controlled thickness and order using surfactant-assisted electrochemical processes, Carbon. N. Y. 50 (1) (2012) 142–152.
[49] S. Claramunt, A. Varea, D. Lopez-Diaz, M.M. Velázquez, A. Cornet, A. Cirera, The importance of interbands on the interpretation of the raman spectrum of graphene oxide, J. Phys. Chem. C. 119 (18) (2015) 10123–10129.
[50] P. Modiba, M. Matoetoe, A.M. Crouch, Kinetics study of transition metal complexes (Ce–DTPA, Cr–DTPA and V–DTPA) for redox flow battery applications, Electrochim. Acta 94 (2013) 336–343.
[51] T. Łuczak, Preparation and characterization of the dopamine film electrochemically deposited on a gold template and its applications for dopamine sensing in aqueous solution, Electrochim. Acta 53 (19) (2008) 5725–5731.
[52] Y. Zheng, Y. Li, Past, Present, Future of tools for Dopamine Detect. Neurosci. 525 (2023) 13–25.
[53] S. Aafria, P. Kumari, S. Sharma, S. Yadav, B. Batra, J.S. Rana, M. Sharma, Electrochemical biosensing of uric acid: a review, Microchem. J. 182 (2022) 107945.
[54] Z. Gazdik, O. Zitka, J. Petrlova, V. Adam, J. Zehnalek, A. Horna, R. Kizek, Determination of vitamin C (ascorbic acid) using high performance liquid chromatography coupled with electrochemical detection, Sensors 8 (11) (2008) 7097–7112.
[55] E.A. McGaw, G.M. Swain, A comparison of boron-doped diamond thin-film and Hg-coated glassy carbon electrodes for anodic stripping voltammetric determination of heavy metal ions in aqueous media, Anal. Chim. Acta 575 (2) (2006) 180–189.
[56] A.Y.S. Eng, A. Ambrosi, C.K. Chua, F. Šanëk, Z. Sofer, M. Pumera, Unusual inherent electrochemistry of graphene oxides prepared using permanganate oxidants, Chem. Eur. J. 19 (38) (2013) 12673–12683.